Journal of Power Sources 431 (2019) 75–83

Contents lists available at ScienceDirect

Journal of Power Sources

journal homepage: www.elsevier.com/locate/jpowsour

Revealing the impacts of metastable structure on the electrochemical properties: The case of MnS

Yanyan Pei [a,b], Chaofeng Liu [a], Zhaoxiang Han [c], Zachary Garbe Neale [a], Wenjing Qian [a], Shuqiang Xiong [a], Zhuwu Jiang [b,**], Guozhong Cao [a,*]

[a] Department of Materials Science and Engineering, University of Washington, Seattle, WA, 98195, USA
[b] College of Ecological Environment and Urban Construction, Fujian University of Technology, Fuzhou, 350118, China
[c] College of Science, China University of Petroleum, Qingdao, 266555, China

ARTICLE INFO

Keywords:
MnS
Metastable structure
Li-ion battery
Capacitor

ABSTRACT

Metastable γ-MnS and stable α-MnS were synthesized via a one-step facile hydrothermal method and investigated as anode materials in Li-ion batteries and capacitors for revealing the essence of their electrochemical difference. Comparing with octahedrally coordinated [MnS_6] in stable α-MnS, the Mn in γ-MnS has a tetrahedral coordination with smaller crystal field splitting and the Mn–S bond with a stronger covalent character, resulting in a lower discharge potential that enables assembled devices with a higher energy density. Density functional theory (DFT) calculation corroborates that the metastable γ-MnS possesses high charge density overlapping in the chemical bonds and decreased energy barriers for the reactive electrons deviating from *3d* orbitals. Metastable γ-MnS delivers a larger storage capacity of 705 mAh g^{-1} at a current density of 100 mA g^{-1}, and also demonstrates superior rate capability (362 mAh g^{-1} at 2 A g^{-1}) and cycling stability (550 mAh g^{-1} remaining after 200 cycles at 0.5 A g^{-1}) in Li-ion half cells. Moreover, the γ-MnS//AC hybrid capacitor with a wide voltage window of 0.1–4 V demonstrates a maximum energy and power density of 220 W h kg^{-1} and 10133 W kg^{-1} respectively, and cycles at 5 A g^{-1} without detectable capacity fading over 5000 cycles.

1. Introduction

With the fast growing demand for high energy and power densities of energy-storage devices for applications such as electric vehicles, and the increased concerns on environmental protection, it is imperative to explore electrode materials capable of a high capacity with high rate capability [1–3]. High-performance electrode materials should have highly reversible storage capacity with rapid redox reactions and fast ion and electron transport capability [4]. Electrodes in lithium-ion batteries (LIBs) convert chemical to electrical energy through one of three redox reactions: intercalation, conversion and alloying [5,6]. The most widely used LIBs electrodes are intercalation materials that reversibly insert/extract lithium ions in/from the active sites in their crystal lattices [7,8]. The capacity of intercalation electrodes is relatively low, as it is limited by the number of crystallographic sites available for reversible insertion/extraction of lithium-ions. The conversion electrodes do not have such limitations and can deliver an order of magnitude higher capacity in comparison with intercalation materials [9]. Though alloying materials such as Sn and Si offer high capacities exceeding 1500 mA h/g, the unavoidable enormous volume expansion during the electrochemical process has hindered their practical usage in commercial LIBs [10–12]. Conversion electrodes offer moderate charge/discharge voltage and large storage capacity, demonstrated to be promising candidates for LiBs and capacitors [13–16].

Fast surface adsorption in capacitors permits a high power density (2–5 kW kg^{-1}), but suffers from relatively low energy density (3–6 W h·kg^{-1}) [17,18]. The accessible strategies to enhance the energy density mainly focus on increasing the operating voltage and charge-storage capacity [9]. Traditional aqueous capacitors have a narrow voltage window because water easily decomposes if the voltage exceeds the limited window of 1.23 V [19,20]. Current research trending in hybrid capacitors is to develop non-aqueous electrolytes with high voltage that effectively solve the problem. [21–23] So much attention is being paid toward increasing the operating voltage of capacitors or developing

* Corresponding author.
** Corresponding author.
E-mail addresses: jiangzhuwu@126.com (Z. Jiang), gzcao@u.washington.edu (G. Cao).

https://doi.org/10.1016/j.jpowsour.2019.05.050
Received 25 January 2019; Received in revised form 13 April 2019; Accepted 12 May 2019
Available online 17 May 2019

advanced electrode materials with high capacity.

Taking those factors into consideration, transition metal sulfides (MS_x) based on conversion reactions with large theoretical Li-ion storage capacity have emerged as desirable electrode materials for both LiBs and capacitors. MS_x possess better mechanical and thermal stability and larger electrical conductivity than those of their corresponding metal oxides (MO_x) [24,25]. The weaker chemical bonding of M–S than that of M–O corresponds to a lower energy barrier for electron transfer in the electrochemical reactions [26]. In addition, the rich redox chemistry that contributes to their large Li-ion storage capacity, even higher than those of carbon/graphite-based materials, make them stand out from other electrode materials [27]. Among available transition metal sulfides, manganese sulfide (MnS) is a promising anode material because of its theoretical specific capacity as high as 616 mA h g^{-1} according to the Gibbs free energy change ($\Delta G = -202.5$ kJ/mol) and electromotive force (emf, E = 1.049 V) [28,29].

MnS is a wide band gap (Eg = 3.7 eV) p-type semiconductor and possesses three types of phases. The α-phase is thermodynamically stable with cubic rock-salt type, while the β and γ-phase are metastable with zinc blende and wurtzite crystal structures, respectively [30]. It is well known that the electrochemical properties of electrode materials are highly dependent on their morphologies and crystal structures. Therefore, MnS micro/nano-structures with various morphologies have been successfully prepared to improve their power density for LIBs or energy density for capacitors [31–34]. For example, MnS microboxes and hollow structured MnS have been synthesized for high-performance electrode materials [35,36].Moreover, much effort such as component modulation and surface modifications with carbonaceous materials have been devoted [37–39]. Zhou et al. prepared branched MnS@C nanochains for LiBs, which showed enhanced electrochemical performance [40]. Recently, the heteroatom doping, especially N, S-doped MnS@C has drawn appealing increasing interests because it can effectively overcome some drawbacks of MnS anode materials such as poor electron transfer rate, low intrinsic electrical conductivity as well as large volume expansion [41]. Although a lot of research has been done with the electrodes for Li-ion batteries, there is a strong and imperative demand for Li-ion batteries with higher energy and power density. For the further advancement of Li-ion batteries, better fundamental understanding of thermodynamics, transport kinetics and electrochemical reactions are obviously needed. Our research intends to achieve a better understanding of the impacts of metastable phase and crystal structure on the electrochemical reactions and transport properties. MnS is rich in different crystal structure and different thermodynamic stability, which were the primary research for us to carry out the basic research presented in this paper.

Herein, both stable α-MnS and metastable γ-MnS were synthesized through a facile hydrothermal method and characterized as conversion electrodes for lithium ion storage in LiBs and capacitors. Metastable γ-MnS displayed a lower discharge potential and exhibited superior rate performance and cycling stability in Li-ion half cells compared with the stable α-phase. DFT calculation corroborate with the experimental data found that γ-MnS possesses high charge density overlapping in chemical bonds and low energy barriers for the reactive electrons deviating from *3d* orbitals. Furthermore, the γ-MnS//AC hybrid capacitor using organic electrolyte ($LiPF_6$) with a high voltage of 4 V demonstrates excellent electrochemical performance with a maximum energy and power density of 220 W h kg^{-1} and 10133 W kg^{-1}, respectively, and cycled at 5 A g^{-1} without detectable capacity fading over 5000 cycles. The excellent properties of metastable structure materials provide an insight for designing desirable electrode materials for high-performance devices.

2. Results and discussion

Fig. 1a shows the XRD patterns of two MnS samples. All reflections can be indexed to standard patterns of MnS. The characteristic diffraction peaks in green correspond to the (111), (200), (220), (311) and (222) planes, which can be indexed to the cubic phase of α-MnS (JCPDS No. 06–0518) with an F*m-3m*(225) space group, and lattice parameter a = 5.22 Å. The diffraction peaks in blue can be indexed with a P63*mc* (186) space group, with lattice parameters a = 3.98 Å, c = 6.45 Å, corresponding to the hexagonal structure of γ-MnS (JCPDS No.40–1289). No impurities or other phases of MnS are detected, indicating high purity of the as-prepared samples. The sharp diffraction peaks of obtained samples indicate high crystallinity of the α-MnS and γ-MnS. According to Scherrer formula:

$$L = K\lambda/\beta cos\theta \quad (1)$$

from strongest peaks (200) and (002), the average size of α-MnS and γ-MnS crystallites is estimated to be 46 nm and 41 nm, respectively. SEM images (Fig. S1) disclose that α-MnS has cubic-like nanoparticles with non-uniform size, and γ-MnS exhibits primarily irregular nanoparticles with similar size ranging in 100–200 nm. From the HRTEM images, it can be clearly identified that α-MnS (Fig. 1c) with lattice spacing of 2.61 Å related to (200) planes, and γ-MnS (Fig. 1d) with lattice spacing of 3.04 Å and 3.22 Å corresponding to (101) and (002) planes, respectively. X-ray energy dispersive spectroscopy (EDS) shows the atomic ratio between Mn and S of the two samples is close to 1:1 (Fig. S2), which is in good agreement with the results of XRD. The N_2 adsorption-desorption isotherms show both α-MnS (Fig. S3) and γ-MnS (Fig. 1b) possess a type III isotherm with similar nonporous structure. No obvious hysteresis loops are observed and the less adsorbed amount implying a weak interaction between N_2 and samples. The surface areas of α-MnS and γ-MnS calculated to be 10.36 and 19.58 m^2 g^{-1}, respectively.

Furthermore, the valence state of Mn ions in resulting samples was analyzed by X-ray photoelectron spectroscopy (XPS) in Fig. 1e-f. The Mn $2p_{3/2}$ and $2p_{1/2}$ main peaks of both samples have the satellite peaks on the higher binding-energy sides, which indicate a strong Coulombic interaction between Mn 3*d* electrons and hybridization between Mn 3*d* and other valence orbitals. Notably, the simulated peaks of Mn $2p_{3/2}$ located at 640.8eV and 641.8eV are both assigned to Mn^{2+}, which is consistent with the chemical valences in both MnS phases as verified through XRD. The separation of binding energy in Mn^{2+} implies that the chemical surroundings around center metal ions and electron distribution in 3*d* orbitals are different. In α-MnS, Mn^{2+} coordinates with six S^{2-} to build a $[MnS_6]$ octahedron, but $[MnS_4]$ tetrahedron is formed in γ-MnS. Under this situation, the electron distribution and the character of chemical bonds are different in both materials, inducing a slight difference in binding energy. More details will be discussed in the following section.

The electrochemical properties of α-MnS and γ-MnS as anode materials for LIBs were investigated. Cyclic voltammograms (CV) were tested for 3 cycles at a scan rate of 0.1 mV s^{-1} in the potential window of 0.01–3.0 V *vs.* Li/Li^+. Fig. 2a shows the CV curves of α-MnS with two obvious peaks during the first cycle. The sharply reduced current and eventual disappearance of the current peak at 0.29 V in the subsequent cycles suggests that this might be an overlapped curve from the conversion reaction of MnS and the decomposition of organic electrolyte. The solvents of electrolyte will obtain electrons and reduced to form a solid electrolyte interphase (SEI) film because the lowest unoccupied molecular orbital (LUMO) of organic solvents lies below the Femi level of metallic Li [26]. The peak centering at 1.32 V corresponds to oxidation of Mn and decomposition of Li_2S. Similarly, the γ-MnS also showed two peaks at 0.24 V and 1.32 V during cathodic and anodic scanning (Fig. 2b) in the first cycle. During the second cycle, the reduction plateau of α-MnS located at 1.6 V could be ascribed to the insertion of Li^+ ions into the MnS crystal lattice to form intermediate Li_xMnS phase. The lower plateau at 0.71 V could be assigned to the conversion process which involves the decomposition of Li_xMnS into Mn nanoparticle distributed into a Li_2S matrix. Meanwhile, the corresponding oxidation peaks at 1.32 V and 1.89 V may be due to the conversion reaction of Mn

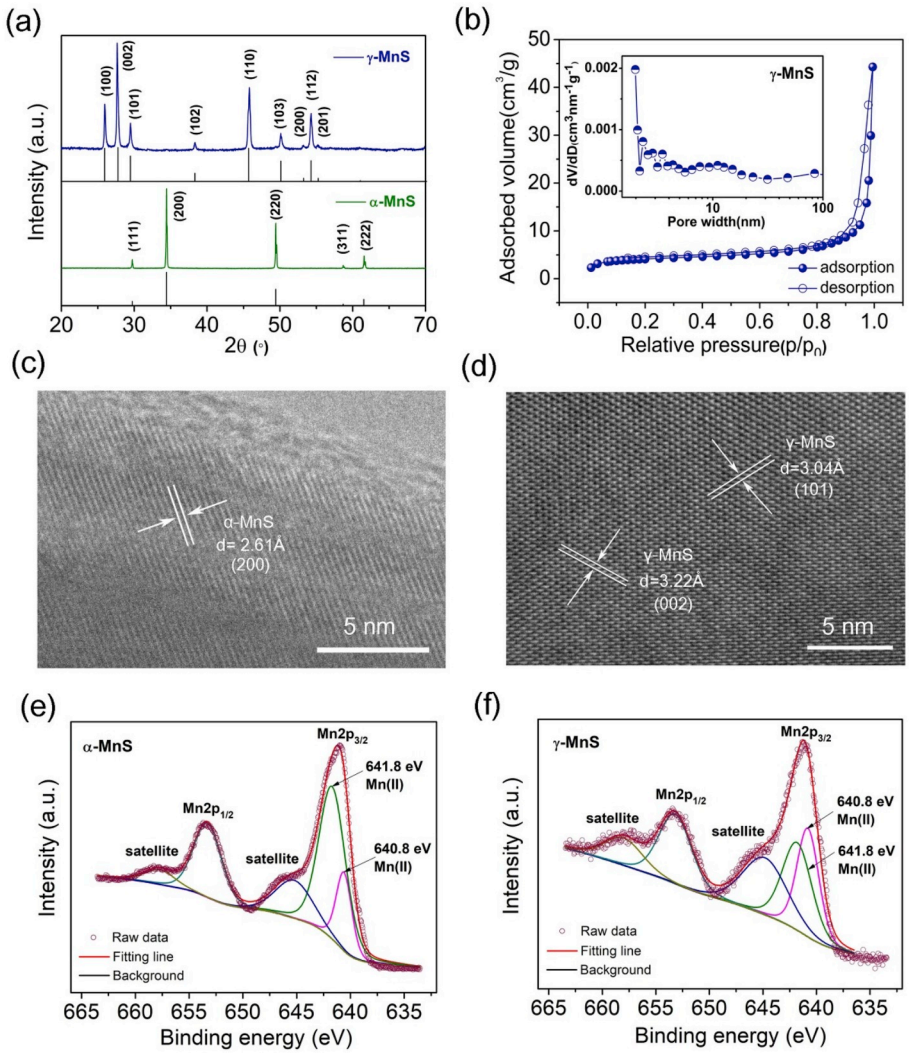

Fig. 1. (a) XRD patterns of two samples, the below green pattern is α-MnS and the upper blue one is γ-MnS. The standard patterns for pure α-MnS (JCPDS No. 06–0518) and pure γ- MnS (JCPDS No.40–1289) are provided at the bottom for comparison. (b) Nitrogen adsorption-desorption curves and pore size distribution of γ-MnS. HRTEM images of (c) α-MnS and (d) γ- MnS. XPS spectra of Mn 2p peaks of (e) α-MnS and (f) γ- MnS. The different binding energy for Mn^{2+} implies the chemical surroundings are distinct in the chemical bonds and the areas suggest the electrons in γ-MnS with a weaker interaction. (For interpretation of the references to colour in this figure legend, the reader is referred to the Web version of this article.)

to Mn^{2+} and Li^+ ions extraction from the MnS lattice process. Thus two pairs of redox process were detected for both α-MnS and γ-MnS from the second cycle, indicating that during charge/discharge the electrochemical reduction and oxidation of MnS may occur in two stages, which is in agreement with previous reports [13,40,42]. Additionally, the minor oxidation peak observed at 2.35 V for both samples is associated with the formation of Li_2S_n ($n > 2$), which emerges until lithium polysulfide is completely consumed during the first few cycles [36,43,44]. The third cycle almost overlapped with the second one, implying the highly reversible electrochemical reactions and excellent cyclability of α-MnS and γ-MnS. As verified in literature [40], the electrochemical reactions involving MnS phases can be described as follows based on the insertion and conversion mechanism with intermediate Li_xMnS phase [45,46].

$$\text{Insertion reaction: } MnS + x\,Li^+ + x\,e^- \leftrightarrow Li_xMnS \quad (2)$$

$$\text{Conversion reaction: } Li_{2-x}MnS + x\,Li^+ + x\,e^- \leftrightarrow Mn + Li_2S \quad (3)$$

The charge/discharge profiles shown in Fig. 2c-d also support the above explanation, two pairs of redox plateaus can be observed for both samples during the first three cycles. The discharge and charge plateaus of the α-MnS electrode are ~0.7 V/0.3 V and ~1.3 V/1.9 V, which is in accordance with the CV results. Notably, the oxidation plateau at 2.35 V attributed to Li_2S_n disappeared gradually from the second cycle, which is in good agreement with the phenomenon in the CV curves. Fig. 2e compares the CVs of γ-MnS at various sweep rates from 0.2 to 1.0 mV s^{-1}. The deviations in redox peaks with increased sweep rates indicate the polarization as reported widely in electrode materials [47,48]. The Li-ion diffusion coefficients in MnS can be calculated from the peak current densities in cathodic and anodic curves at various scanning rates based on the Randles-Sevchik equation.

$$I_p = 0.4463\left(\frac{F^3}{RT}\right)^{1/2} n^{3/2} A D^{1/2} C_0 v^{1/2} \quad (4)$$

where I_p is the peak current (A), R is the gas constant (8.314 J mol^{-1} K^{-1}), T (K) is the absolute temperature, F is the Faraday constant (96500 C mol^{-1}), n is the number of electrons transferred per molecule (2), A is the active surface area of the electrode (0.785 cm^2), C_0 is the concentration of Li ions in the electrolyte (1.0×10^{-3} mol cm^{-3}), D is the apparent ion diffusion coefficient (cm^2 s^{-1}), and v is the scanning rate (V s^{-1}). From the slopes of the fitting lines shown in Fig. 2f, the obtained Li ions diffusion coefficients (D) of γ-MnS are 6.2×10^{-10} and 9.0×10^{-9} cm^2 s^{-1} for anodic and cathodic process, which are larger than 5.2×10^{-10} and 5.0×10^{-9} cm^2 s^{-1} in α-MnS (Fig. S4). The higher diffusion coefficient in γ-MnS indicates that the metastable layer structure facilitates Li^+ diffusion and further accelerates redox reactions. Fig. 2g presents the rate capability of MnS with current density increased stepwise from 0.1 to 2 A g^{-1}. It is obvious that the overall specific capacity of α-MnS is lower than that of γ-phase. In the initial cycle, α-MnS and γ-MnS delivered a discharge capacity of 1033 and 939 mA h g^{-1} at a

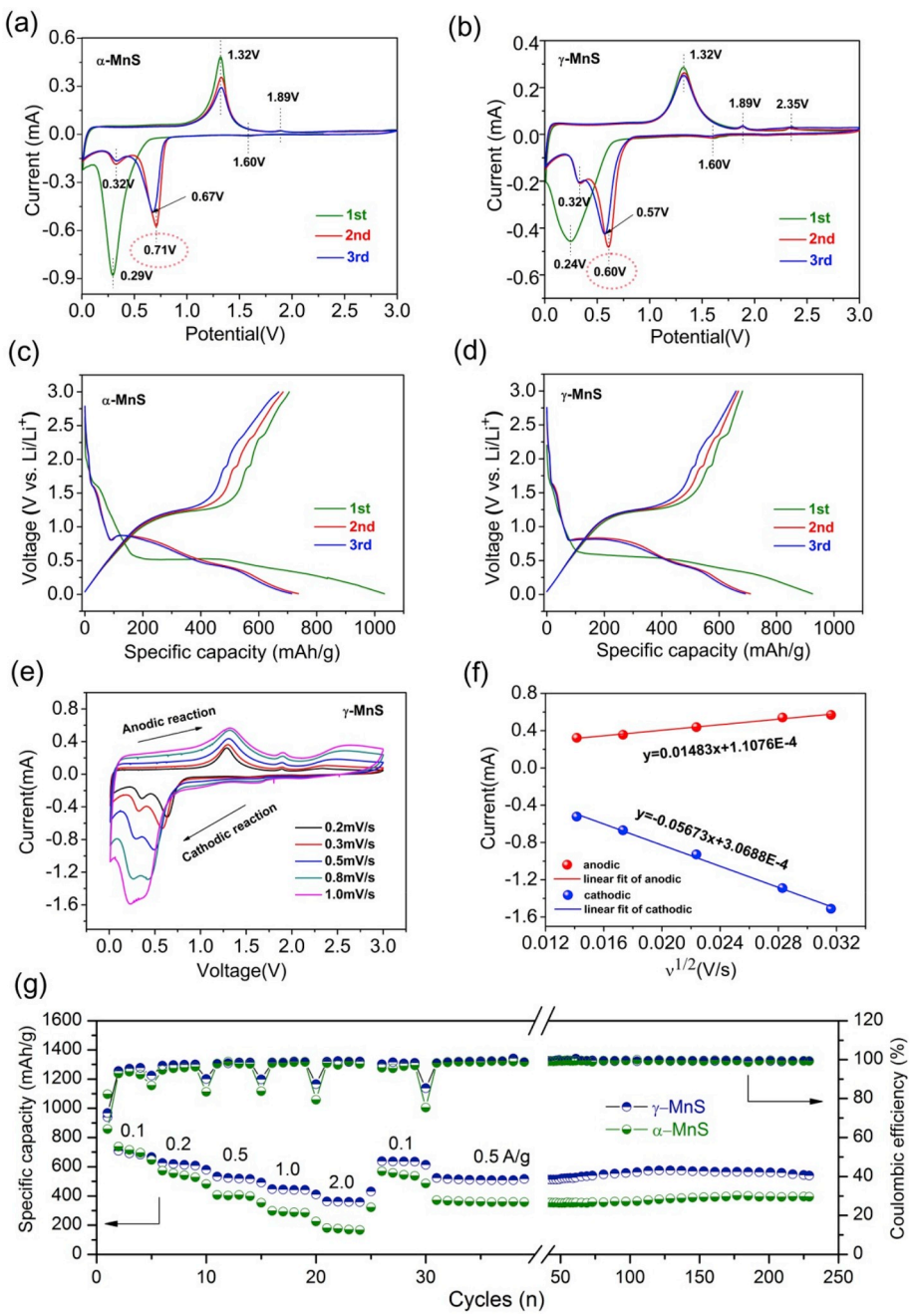

Fig. 2. CV curves of (a) α-MnS and (b) γ-MnS at a scan rate of 0.1 mVs^{-1} with the voltage window of o. o1-3 V. Galvanostatic discharge-charge profiles of (c) α-MnS and (d) γ-MnS for the first three cycles at a current density of 0.1 A g^{-1}; (e) CVs curves of γ-MnS measured at various current densities and the deviations in redox peaks indicate the polarization. (f) Relationship between peak currents and scanning rates. The slope of the fitting linear can be used to calculate the Li-ion diffusion coefficient. (g) Rate performance of both samples measured with different current densities and cycling stability tested at 0.5 A g^{-1} for 200 cycles after rate tests.

current density of 0.1 A g^{-1}. The corresponding Coulombic efficiency is 64% and 73%, respectively. The low initial Coulombic efficiency can be attributed to the formation of the SEI layer and the by-products known as poly-sulfides, causing shuttled and dissolved effects [27,49]. The higher Coulombic efficiency from γ-MnS means that less and weaker side reactions happened during the discharging process. In the second cycle, the Coulombic efficiency almost increased to 100%, implying the formed SEI inhibits the following possible side reaction at the interface between electrode materials and electrolyte. The reversible charge capacity of γ-MnS decreased only slightly during the first 5 cycles while the capacity of α-MnS drops severely from 705 to 560 mAh g^{-1}. Even being tested at 2.0 A g^{-1}, the capacity of γ-MnS can still reach 362 mAh g^{-1} and recovers to 638 mAh g^{-1} when the current density returns to 0.1 A g^{-1}. Moreover, the cycling performances of two samples at a current density of 0.5 A g^{-1} still carried out after rate tests. As it is shown in Fig. 2g, the capacity of γ-MnS increased slightly after 50 cycles and then stabilized at 550 mAh g^{-1} thereafter. The increase in capacity might be from electrolyte decomposition that leads to a gel-like polymeric layer which enables additional lithium storage in a capacitive way, as reported by many other conversion materials [50,51]. The capacity of α-MnS also exhibits unperceivable degradation and maintains at 395 mAh g^{-1} till 200 cycles. Overall the metastable γ-MnS displayed much better rate performance and cycling stability than those of α-phase and other transition metal sulfide, such as CoS_2 [52] and MoS_2 [13] under the same current densities. In addition, cycling performances of α-MnS and γ-MnS at a current density of 0.1 A g^{-1} and electrochemical impedance spectra (EIS) of the cells were collected before and after 50 cycles (Fig. S5) for better understanding of electrochemical performances. The metastable γ-MnS exhibits better cycling stability and lower charge transfer resistance compared with α-phase. The charge transfer resistance decreased after 50 cycles, indicating a faster electronic transfer during cycling [43,53,54]. Fig. S6 also exhibits TEM

images of α-MnS and γ-MnS electrodes after cycling, the overall crystal size remained almost the same with the initial morphology, indicating that the metastable structure has well accommodated the volume expansion and corresponding stress during cycling.

Compared with the stable α-MnS, it is worth noting that the metastable γ-MnS exhibits a lower discharge voltage profile during the conversion process as verified in CV and galvanostatic voltage-capacity curves. According to Nernst equation, the Gibbs free energy change can give an electrochemical potential of redox reaction that is the open circuit voltage of a cell. Considering that the nature of the conversion reaction is the breaking and recombination of chemical bond, and the chemical bond dissociation energy (BDE) belongs to chemical enthalpy change, the Gibbs free energy change in the conversion reaction could be defined as:

$$\Delta G_{MnS} = \Delta H_{BDE} + P\Delta V - T\Delta S \quad (5)$$

Normally, the values of $P\Delta V$ and $T\Delta S$ in the conversion reaction are negligible compared with that of ΔH_{BDE} [26,55]. Thus the change of chemical bond dissociation energy approximates to Gibbs free energy change, and can be used roughly to estimate the discharge voltage by the following equation:

$$\Delta G_{MnS} = -nFE_{MnS} \approx (\Delta H_{Mn-Mn} + 2\Delta H_{Li-s}) - (\Delta H_{Mn-s} + 2\Delta H_{Li-Li}) \quad (6)$$

The bond dissociation energies of Mn–S, Li–Li, Mn–Mn and Li–S are 301, 106, 42 and 269 kJ/mol [56], respectively. The calculated ΔG_{MnS} is 88.6 kJ/mol indicating MnS has a discharge potential of 0.46 V. This calculated result approaches to the experimental results but with a slight difference owing to the chemical surroundings, the electron state and character of chemical bonds are not considered. Fig. 3a-b shows the chemical coordination of Mn^{2+} in both phases. [MnS_6] octahedrons form in the stable α-MnS, but Mn^{2+} coordinates into [MnS_4] tetrahedrons in the metastable γ-MnS. The difference in the coordination surroundings will influence the crystal field strength and the degeneration state in the 3*d* orbitals of center metal ion. Due to the octahedron symmetry in thermodynamically stable α-MnS (Fig. 3c), the repulsion between the electrons in 3*d* orbitals of Mn^{2+} and ligand S^{2-} causes a loss of degeneracy. Then there appears two sets of orbitals, one is t_{2g} that is the lower-energy orbital and includes d_{xy}, d_{yz} and d_{xz}. The other is e_g, it belongs to the higher-energy orbital that includes d_z^2 and d_{x-y}^{22}. S^{2-} is a weak-field ligand, it coordinates with the center metal ion Mn^{2+} to form a high spin occupation state, so the five electrons occupy five different orbitals. In tetrahedron symmetry, 3*d* orbitals split into the similar two sets, but e_g is the lower-energy orbitals and t_{2g} converses to higher-energy orbitals (Fig. 3d). More importantly, the tetrahedral crystal field splitting energy is roughly equal to 4/9 of that in the octahedral crystal field. The energy position of e_g in the tetrahedron (metastable γ-MnS) is higher than the t_{2g} in the octahedron (stable α-MnS). In the discharging process of the metastable γ-MnS, Mn^{2+} is reduced to metallic Mn, the two incoming electrons will enter into the lower-energy orbitals in both 3*d* orbitals to decrease the system energy. Obviously, the relatively higher-energy orbitals in the tetrahedron of metastable γ-MnS will induce a smaller energy change in the whole system. The smaller energy change means a lower discharging voltage that strongly supports the argument from the CV curves and galvanostatic discharging voltages. When the Mn^{2+} is conversed to Mn, the 3*d* and 4*s* orbitals have the same situation in both phases. In the charging process, metallic Mn will lose the two 4s electrons first, so the energy change at this step is same in both phases. This is the reason why both phase displayed the same oxidizing voltages in the CV curves. Charge density difference maps from DFT calculation of α-MnS and γ-MnS (Fig. 3e–f) show the electron distribution in the chemical bonds. The 3*d* electrons in Mn^{2+} is separated with the electrons in S^{2-} in the stable α-MnS, however, a remarkable overlapping can be observed between Mn^{2+} and S^{2-} in the chemical bond of the metastable γ-MnS. Those indicate the stable α-MnS has a strong ionic character in chemical bonds but metastable γ-MnS exhibits a remarkable covalent character. Thus,

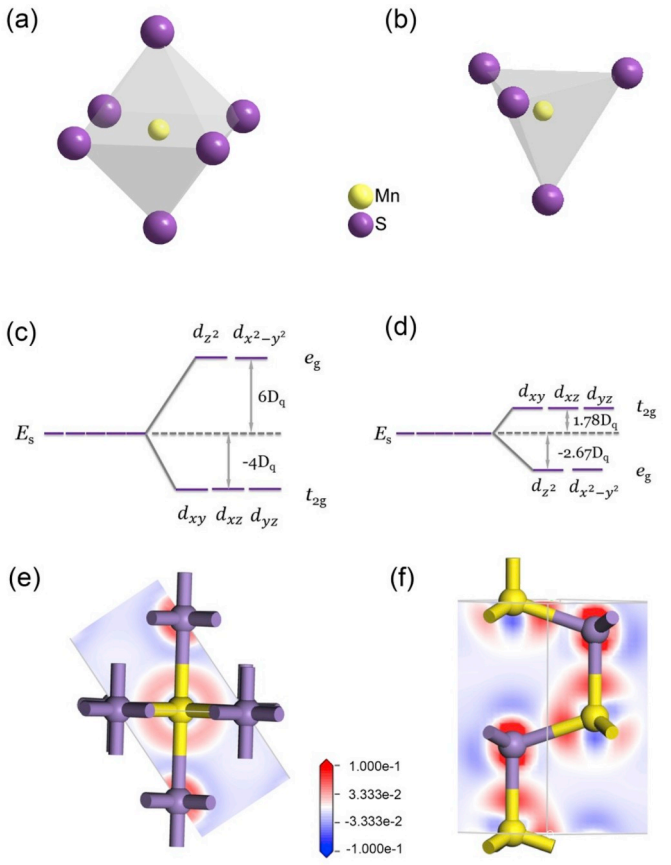

Fig. 3. Chemical coordination of Mn^{2+} in both phases (a) [MnS_6] octahedron in α-MnS and (b) [MnS_4] tetrahedron in γ-MnS. The 3*d* orbitals split into two sets in crystal field, one is t_{2g} that includes d_{xy}, d_{xz} and d_{yz}, the other is e_g that consists of d_z^2 and d_{x-y}^{22}. (c) Crystal field splitting of 3*d* orbitals of Mn ions in octahedral symmetry of α-MnS, e_g belongs to the higher-energy orbital and t_{2g} is the lower-energy orbitals. (d) The 3*d* orbitals of Mn ions in tetrahedral symmetry of γ-MnS have an opposite situation, the energy difference between two sets of orbitals is roughly equal to 4/9 of that in octahedral symmetry. Charge density difference maps from DFT calculation of (e) α-MnS and (f) γ-MnS. The electrons in metal ion and ligand has an overlapping in γ-MnS, but are totally separated in α-MnS, demonstrating a strong covalent character in γ-MnS and ionic character in α-MnS.

electrons in 3*d* orbitals possess higher energy in the metastable γ-MnS than that in the stable α-MnS. It strongly supports the arguments from crystal filed theory discussed above and verifies the four-coordinated metastable γ-MnS has a lower discharging voltage. In addition, the character of chemical bonds influences the actual dissociation energy in different crystal structures, while the bond energies used in the calculation from the handbook are the average values. Therefore, the results demonstrate the voltage calculation from chemical bond dissociation energy should consider the impacts from electron configuration in orbitals or chemical bonds.

Apart from the difference in the displayed discharge voltages, metastable γ-MnS also presents superior rate capability and cycling performance owing to the lower energy barrier for faster ion diffusion and highly reversible phase transition for electrochemical reactions. From the energetics point, γ-MnS possesses a higher Gibbs free energy (G*) and larger unit cell volume as it is less stable than α-MnS (Table S1). According to literature [57], the larger unit cell volume corresponds to smaller lattice energy, condensation energy or internal energy, which facilitates Li ions to intercalate into the metastable layered structure of γ-phase. Beside those, the higher Gibbs free energy in γ-MnS may also provide a driving force for highly reversible phase transition during conversion reaction. The *ex situ* XRD patterns in Fig. 4 showed that both

α-MnS and γ-MnS retained their original crystalline structure during cycling. It can be observed that the characteristic peaks (100), (002), (101) of γ-MnS decreased obviously but still left a little "trace" at the end of the discharge process. When the charge proceeded, the peaks of MnS are recovered with strong intensities comparable to that of the pristine MnS phase. The reasonable explanation is the partial transformation of crystalline to amorphous structure due to incomplete lithiation/delithiation. It is possible that the polarization at the late stage prevents the complete phase transition. The "trace" crystallinity served as a crystal seed, inducing the crystalline-phase formation in the charge process. Such "memory effect" of MnS during conversion reaction is of great benefit, which endows the γ-phase to retain all the advantages of metastable structure and highly reversibility in electrochemical reactions. The absence of any characteristic peaks of Mn and Li_2S may well be attributed to the possible amorphous nature of Mn and Li_2S. Namely, the resulting products may either have very small crystallites or are amorphous so that it was reflected as the broad peak in the XRD patterns. Latest work [38,45] also reported this phenomenon and some possible phase transformation mechanisms are being proposed, further investigations using *in-situ* XRD/TEM or other convincing evidence needs to be provided to study the phase transformation mechanisms comprehensively. More detailed work will be done in the future.

Apart from the electrochemical properties in Li-ion half cells, metastable MnS was further employed as an anode in Li-ion hybrid capacitors with an activated carbon (AC) cathode. The AC possesses a specific surface area of ~1800 $m^2 g^{-1}$ and was used in our previous work [58]. The active mass ratio was set at 1:6 between anode and cathode to ensure the charge balance in both electrodes. The galvanostatic charge/discharge (GCD) curves at various current densities in the potential window of 0.1–4 V are depicted in Fig. 5a-b. Evidently, all GCD curves are nonlinear and the shapes exhibit typical pseudocapacitive characteristics, and no obvious voltage drop at the initial discharge curves, indicating that metastable MnS have low internal ohmic resistance and good electrochemical capacitive behavior. It is worth noting that the charging voltage of this hybrid capacitor can reach up to 4.0 V, demonstrating the potential window can be easily extended using a non-aqueous asymmetric system and a lower discharging potential anode. Compared with α-MnS, the longer discharge time (7156 s at 0.2 A g^{-1}) of γ-MnS suggests the better storage feature with excellent Coulombic efficiency (above 95%), which is important for the practical application in energy storage. As shown in Fig. 5c, the discharge capacity of γ-MnS//AC was ranged from 441 to 132 mAh g^{-1}, higher than α-MnS//AC ranging from 384 to 82 mAh g^{-1} at different current densities (0.1–12.8 A g^{-1}). It also could return to the initial values when the current density was set back to 0.1 A g^{-1}, indicating the better reversibility of redox reactions. The γ-MnS//AC hybrid capacitor also demonstrate remarkable competitive advantages in comparison with $Ni_{1.77}Co_{1.23}S_4$//AC [59] or MnO//AC [60] Li-ion capacitors. Furthermore, the long-term cyclic stability of γ-MnS//AC is much better than that of α-MnS//AC (Fig. 5e), and the higher specific capacity means better reversibility of metastable structure. The specific capacitance of γ-MnS//AC decreased slightly first then increased with a stable retention thereafter, no detectable capacity decay over 5000 cycles. Kinetics changes at the interface and structure degradation could contribute to the fading capacitance. The increased capacitance can be ascribed to the materials activation of the internal material of particles and the reduced particle size increased the interfacial surface area, which could favor Li^+/electron transport and interfacial charge storage, similar to the verified results reported in NiS electrode [34]. The Ragone plots are displayed in Fig. 5d, the achieved maximum energy and power density in γ-MnS//AC capacitor can reach up to 220 W h kg^{-1} and 10133 W kg^{-1}, respectively, higher than those of α-MnS//AC capacitor (172 W h kg^{-1}, 7680 W kg^{-1}). These values are competitive to those of MnS (52 W h kg^{-1}, 1233 W kg^{-1}) [38], ZnS (51 W h kg^{-1}, 822 W kg^{-1}) [61], Cu_7S_4 (35 W h kg^{-1}, 602 W kg^{-1}) [62], MoS_2 (17 W h kg^{-1}, 128 W kg^{-1}) [63] and carbon/graphene based symmetrical supercapacitors [64,65], and even comparable to those of some asymmetric systems such as MnO_2/Ti_3C_2//AC (8.3 W h kg^{-1}, 2376 W kg^{-1}) [14], TiO_2-rGO//AC (42 W h kg^{-1}, 8000 W kg^{-1}) [66], mNb_2O_5–C//AC (48 W h kg^{-1}, 14164 W kg^{-1}) [67] with a voltage window of 1.0–3.0 V. Compared with both symmetrical capacitors and asymmetrical capacitors, this γ-MnS//AC hybrid capacitor undoubtedly displayed both high energy and power densities due to its wider voltage window and unique metastable structure.

3. Conclusions

Both stable α-MnS and metastable γ-MnS were investigated as anode materials for Li-ion batteries and capacitors. DFT results corroborate with the experimental data that the metastable γ-MnS possesses a weaker covalent bond and smaller crystal field splitting, resulting in a lower discharge potential and exhibited superior rate performance and

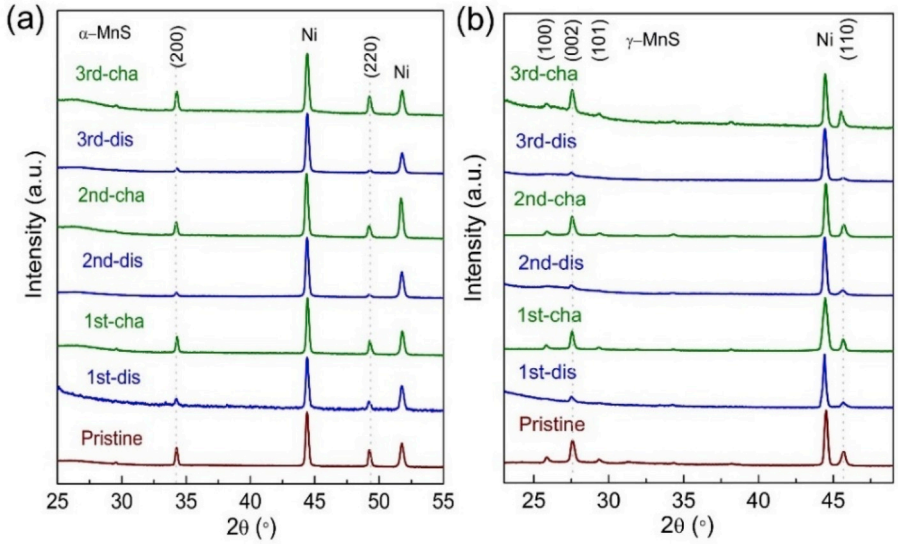

Fig. 4. *ex situ* XRD patterns of (a) α-MnS and (b) γ-MnS electrodes at various charge/discharge states in initial three cycles. At the discharging process, the main peaks become weak and almost disappeared because the conversion reaction leads to the phase transition of MnS, but the crystal structure recovers after the full charging. The residue pristine phase works as the crystallite core that keeps the regeneration of the phases in the electrochemical processes.

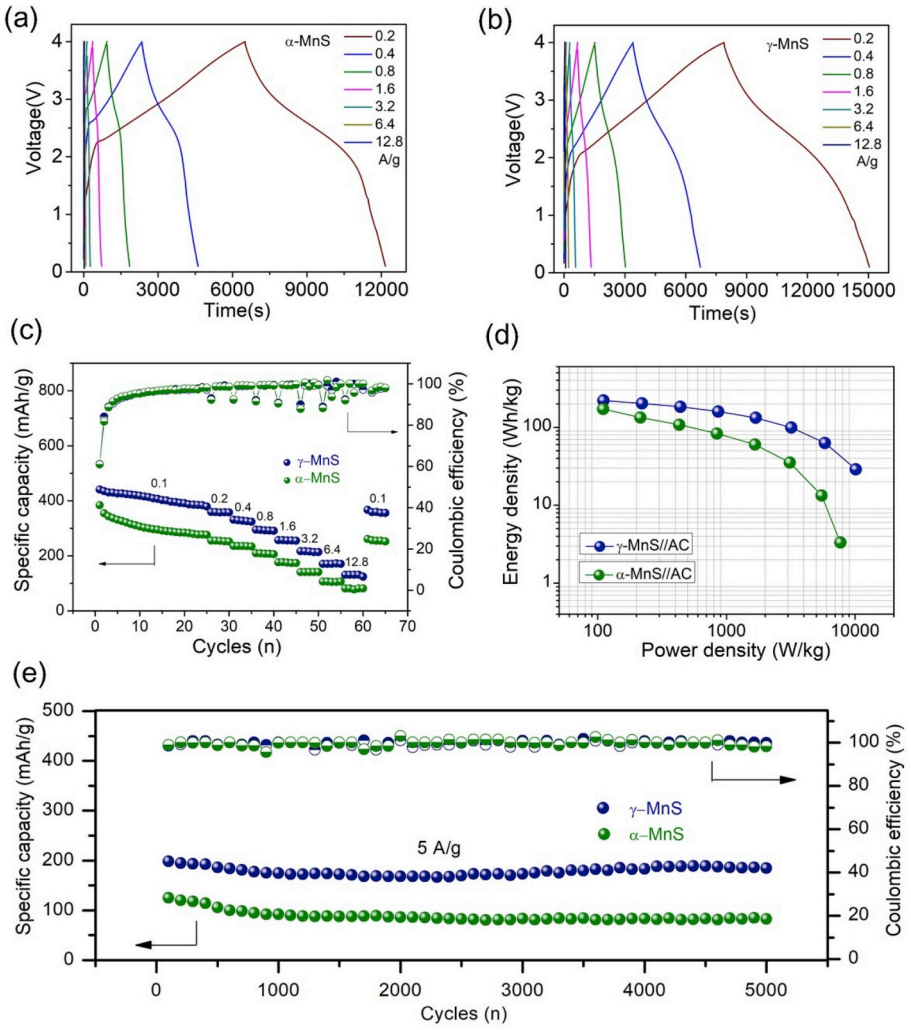

Fig. 5. Profile of charge/discharge curves of (a) α-MnS//AC and (b) γ-MnS//AC hybrid capacitors. (c) Rate performance of both hybrid capacitors measured with different current densities in the voltage potential of 0.1–4.0 V. (d) Ragone plot of both samples fabricated as hybrid capacitors. The data is calculated on the total active mass in both electrodes. (e) Cycling stability of both hybrid capacitors tested at 5 Ag-1 over 5000 cycles after rate tests.

cycling stability in Li-ion half cells in comparison with the stable α-phase. Metastable γ-MnS delivers a larger storage capacity of 705 mAh g^{-1} at a current density of 100 mA g^{-1}, and also demonstrates superior rate capability (362 mAh g^{-1} at 2 A g^{-1}) and cycling stability (550 mAh g^{-1} remaining after 200 cycles at 0.5 A g^{-1}). Moreover, the metastable γ-MnS//AC hybrid capacitor with a wide voltage window of 0.1–4 V demonstrates a maximum energy and power density of 220 W h kg^{-1} and 10133 W kg^{-1}, respectively, and cycles at 5 A g-1 without detectable retention over 5000 cycles. The fundamental consideration with the supported results are helpful for exploiting high-performance electrode materials, and the promising metastable materials present a competitive capability for practical applications in the future.

Notes

The authors declare no competing financial interest.

Acknowledgements

This work was supported by the National Science Foundation (DMR No.1505902) and National Natural Science Foundation of China (No. 51878171),the Research Start-up Funds of Fujian University of Technology (GY-Z19043). Part of this work was conducted at the Molecular Analysis Facility, a National Nanotechnology Coordinated Infrastructure site at the Clean Energy Institute in University of Washington (Grant ECC1542101). The first author also highly appreciates the financial support from the China Scholarship Council (CSC No. 201606270073) for the study in University of Washington.

Appendix A. Supplementary data

Supplementary data to this article can be found online at https://doi.org/10.1016/j.jpowsour.2019.05.050.

References

[1] K. Kang, Y.S. Meng, J. Bréger, C.P. Grey, G. Ceder, Electrodes with high power and high capacity for rechargeable lithium batteries, Science 311 (5763) (2006) 977.
[2] V. Etacheri, R. Marom, R. Elazari, G. Salitra, D. Aurbach, Challenges in the development of advanced Li-ion batteries: a review, Energy Environ. Sci. 4 (9) (2011) 3243.
[3] C.N. Schmidt, G. Cao, Properties of mesoporous carbon modified carbon felt for anode of all-vanadium redox flow battery, Science China Materials 59 (12) (2016) 1037–1050.
[4] P.R. Bandaru, H. Yamada, R. Narayanan, M. Hoefer, Charge transfer and storage in nanostructures, Mater. Sci. Eng. R Rep. 96 (2015) 1–69.
[5] C. Liu, G. Cao, Fundamentals of rechargeable batteries and electrochemical potentials of electrode materials, in: D. Wang, G. Cao (Eds.), Nanomaterials for Energy Conversion and Storage, WORLD SCIENTIFIC (EUROPE), 2017, pp. 397–451.
[6] M. Armand, J.M. Tarascon, Building better batteries, Nature 451 (7179) (2008) 652–657.

[7] M. Winter, J.O. Besenhard, M.E. Spahr, P. Novák, Insertion electrode materials for rechargeable lithium batteries, Adv. Mater. 10 (10) (1998) 725–763.
[8] R.C. Massé, C. Liu, Y. Li, L. Mai, G. Cao, Energy storage through intercalation reactions: electrodes for rechargeable batteries, National Science Review 4 (1) (2017) 26–53.
[9] A. Manthiram, An outlook on lithium ion battery technology, ACS Cent. Sci. 3 (10) (2017) 1063–1069.
[10] Y.-M. Chiang, Building a better battery, Science 330 (6010) (2010) 1485.
[11] Y. Idota, T. Kubota, A. Matsufuji, Y. Maekawa, T. Miyasaka, Tin-based amorphous oxide: a high-capacity lithium-ion-storage material, Science 276 (5317) (1997) 1395.
[12] J. Xu, P. Gu, J. Zhang, H. Xue, H. Pang, Copper-based nanomaterials for high-performance lithium-ion batteries, Part. Part. Syst. Char. 33 (11) (2016) 784–810.
[13] L. Zhang, H.B. Wu, Y. Yan, X. Wang, X.W. Lou, Hierarchical MoS2 microboxes constructed by nanosheets with enhanced electrochemical properties for lithium storage and water splitting, Energy Environ. Sci. 7 (10) (2014) 3302–3306.
[14] W. Liu, Z. Wang, Y. Su, Q. Li, Z. Zhao, F. Geng, Molecularly stacking manganese dioxide/titanium carbide sheets to produce highly flexible and conductive film electrodes with improved pseudocapacitive performances, Advanced Energy Materials 7 (22) (2017) 1602834.
[15] Y. Zhong, M. Yang, X. Zhou, Y. Luo, J. Wei, Z. Zhou, Orderly packed anodes for high-power lithium-ion batteries with super-long cycle life: rational design of MnCO3/large-area graphene composites, Adv. Mater. 27 (5) (2015) 806–812.
[16] Y. Zhang, P. Chen, X. Gao, B. Wang, H. Liu, H. Wu, H. Liu, S. Dou, Nitrogen-doped graphene ribbon assembled core–sheath MnO@graphene scrolls as hierarchically ordered 3D porous electrodes for fast and durable lithium storage, Adv. Funct. Mater. 26 (43) (2016) 7754–7765.
[17] J. Han, L.L. Zhang, S. Lee, J. Oh, K.-S. Lee, J.R. Potts, J. Ji, X. Zhao, R.S. Ruoff, S. Park, Generation of B-doped graphene nanoplatelets using a solution process and their supercapacitor applications, ACS Nano 7 (1) (2013) 19–26.
[18] W. Qian, F. Sun, Y. Xu, L. Qiu, C. Liu, S. Wang, F. Yan, Human hair-derived carbon flakes for electrochemical supercapacitors, Energy Environ. Sci. 7 (1) (2014) 379–386.
[19] S. Xiong, J. Fan, Y. Wang, J. Zhu, J. Yu, Z. Hu, A facile template approach to nitrogen-doped hierarchical porous carbon nanospheres from polydopamine for high-performance supercapacitors, J. Mater. Chem. 5 (34) (2017) 18242–18252.
[20] L.L. Zhang, X.S. Zhao, Carbon-based materials as supercapacitor electrodes, Chem. Soc. Rev. 38 (9) (2009) 2520–2531.
[21] M. Zhi, C. Xiang, J. Li, M. Li, N. Wu, Nanostructured carbon-metal oxide composite electrodes for supercapacitors: a review, Nanoscale 5 (1) (2013) 72–88.
[22] Q. Wang, Z.H. Wen, J.H. Li, A hybrid supercapacitor fabricated with a carbon nanotube cathode and a TiO2–B nanowire anode, Adv. Funct. Mater. 16 (16) (2006) 2141–2146.
[23] Y. Wang, Y. Song, Y. Xia, Electrochemical capacitors: mechanism, materials, systems, characterization and applications, Chem. Soc. Rev. 45 (21) (2016) 5925–5950.
[24] M.R. Harrison, M.G. Francesconi, Mixed-metal one-dimensional sulfides—a class of materials with differences and similarities to oxides, Coord. Chem. Rev. 255 (3–4) (2011) 451–458.
[25] X. Xu, W. Liu, Y. Kim, J. Cho, Nanostructured transition metal sulfides for lithium ion batteries: progress and challenges, Nano Today 9 (5) (2014) 604–630.
[26] C.F. Liu, Z.G. Neale, G.Z. Cao, Understanding electrochemical potentials of cathode materials in rechargeable batteries, Mater. Today 19 (2) (2016) 109–123.
[27] X. Rui, H. Tan, Q. Yan, Nanostructured metal sulfides for energy storage, Nanoscale 6 (17) (2014) 9889–9924.
[28] P. Poizot, S. Laruelle, S. Grugeon, J.M. Tarascon, Rationalization of the low-potential reactivity of 3d-metal-based inorganic compounds toward Li, J. Electrochem. Soc. 149 (9) (2002) A1212.
[29] J.M. Yan, H.Z. Huang, J. Zhang, Z.J. Liu, Y. Yang, A study of novel anode material CoS2 for lithium ion battery, J. Power Sources 146 (1–2) (2005) 264–269.
[30] S.C. Riha, A.A. Koege, X.B. Meng, I.S. Kim, Y.Q. Cao, M.J. Pellin, J.W. Elam, A.B. F. Martinson, Atomic layer deposition of MnS: phase control and electrochemical applications, Acs Appl Mater Inter 8 (4) (2016) 2774–2780.
[31] Y.-w. Jun, Y.-y. Jung, J. Cheon, Architectural control of magnetic semiconductor nanocrystals, J. Am. Chem. Soc. 124 (4) (2002) 615–619.
[32] S. Lei, K. Tang, Q. Yang, H. Zheng, Solvothermal synthesis of metastable γ-MnS hollow spheres and control of their phase, Eur. J. Inorg. Chem. 2005 (20) (2005) 4124–4128.
[33] Y. Zheng, Y. Cheng, Y. Wang, L. Zhou, F. Bao, C. Jia, Metastable γ-MnS hierarchical Architectures: synthesis, characterization, and growth mechanism, J. Phys. Chem. B 110 (16) (2006) 8284–8288.
[34] X.-Y. Yu, L. Yu, L. Shen, X. Song, H. Chen, X.W.D. Lou, General formation of MS (M = Ni, Cu, Mn) box-in-box hollow structures with enhanced pseudocapacitive properties, Adv. Funct. Mater. 24 (47) (2014) 7440–7446.
[35] X.J. Xu, S.M. Ji, M.Z. Gu, J. Liu, In situ synthesis of MnS hollow microspheres on reduced graphene oxide sheets as high-capacity and long-life anodes for Li- and Na-ion batteries, Acs Appl Mater Inter 7 (37) (2015) 20957–20964.
[36] L. Zhang, L. Zhou, H.B. Wu, R. Xu, X.W. Lou, Unusual formation of single-crystal manganese sulfide microboxes co-mediated by the cubic crystal structure and shape, Angew Chem. Int. Ed. Engl. 51 (29) (2012) 7267–7270.
[37] J. Beltran-Huarac, O. Resto, J. Carpena-Nunez, W.M. Jadwisienczak, L.F. Fonseca, B.R. Weiner, G. Morell, Single-crystal gamma-MnS nanowires conformally coated with carbon, Acs Appl Mater Inter 6 (2) (2014) 1180–1186.
[38] M.S. Javed, X. Han, C. Hu, M. Zhou, Z. Huang, X. Tang, X. Gu, Tracking pseudocapacitive contribution to superior energy storage of MnS nanoparticles grown on carbon textile, ACS Appl. Mater. Interfaces 8 (37) (2016) 24621–24628.
[39] X. Li, J. Shen, N. Li, M. Ye, Fabrication of γ-MnS/rGO composite by facile one-pot solvothermal approach for supercapacitor applications, J. Power Sources 282 (2015) 194–201.
[40] J.Y. Ning, D. Zhang, H.H. Song, X.H. Chen, J.S. Zhou, Branched carbon-encapsulated MnS core/shell nanochains prepared via oriented attachment for lithium-ion storage, J. Mater. Chem. 4 (31) (2016) 12098–12105.
[41] D.H. Liu, W.H. Li, Y.P. Zheng, Z. Cui, X. Yan, D.S. Liu, J. Wang, Y. Zhang, H.Y. Lu, F.Y. Bai, J.Z. Guo, X.L. Wu, Situ encapsulating alpha-MnS into N,S-codoped nanotube-like carbon as advanced anode material: alpha–> beta phase transition promoted cycling stability and superior Li/Na-storage performance in half/full cells, Adv. Mater. 30 (21) (2018) e1706317.
[42] N. Mahmood, C. Zhang, Y. Hou, Nickel sulfide/nitrogen-doped graphene composites: phase-controlled synthesis and high performance anode materials for lithium ion batteries, Small 9 (8) (2013) 1321–1328.
[43] K.M. Jeon, J.S. Cho, Y.C. Kang, Electrochemical properties of MnS-C and MnO-C composite powders prepared via spray drying process, J. Power Sources 295 (2015) 9–15.
[44] G.Y. Li, B.H. He, M.J. Zhou, G.X. Wang, N.B. Zhou, W.Y. Xu, Z.H. Hou, Solvothermal synthesis of mesoporous manganese sulfide nanoparticles supported on nitrogen and sulfur Co-doped graphene with superior lithium storage performance, Chemelectrochem 4 (1) (2017) 81–89.
[45] Y. Hao, C.H. Chen, X.Y. Yang, G.J. Xiao, B. Zou, J.W. Yang, C.L. Wang, Studies on intrinsic phase-dependent electrochemical properties of MnS nanocrystals as anodes for lithium-ion batteries, J. Power Sources 338 (2017) 9–16.
[46] Y. Liu, Y. Qiao, W.X. Zhang, Z. Li, X.L. Hu, L.X. Yuan, Y.H. Huang, Coral-like alpha-MnS composites with N-doped carbon as anode materials for high-performance lithium-ion batteries, J. Mater. Chem. 22 (45) (2012) 24026–24033.
[47] C.F. Liu, C.K. Zhang, H.Y. Fu, X.H. Nan, G.Z. Cao, Exploiting high-performance anode through tuning the character of chemical bonds for Li-ion batteries and capacitors, Advanced Energy Materials 7 (1) (2017).
[48] X. Zhao, H.-E. Wang, R.C. Massé, J. Cao, J. Sui, J. Li, W. Cai, G. Cao, Design of coherent anode materials with 0D Ni3S2 nanoparticles self-assembled on 3D interconnected carbon networks for fast and reversible sodium storage, J. Mater. Chem. 5 (16) (2017) 7394–7402.
[49] N. Jayaprakash, J. Shen, S.S. Moganty, A. Corona, L.A. Archer, Porous hollow carbon@sulfur composites for high-power lithium-sulfur batteries, Angew Chem. Int. Ed. Engl. 50 (26) (2011) 5904–5908.
[50] Y.Y. Hu, Z. Liu, K.W. Nam, O.J. Borkiewicz, J. Cheng, X. Hua, M.T. Dunstan, X. Yu, K.M. Wiaderek, L.S. Du, K.W. Chapman, P.J. Chupas, X.Q. Yang, C.P. Grey, Origin of additional capacities in metal oxide lithium-ion battery electrodes, Nat. Mater. 12 (12) (2013) 1130–1136.
[51] A. Ponrouch, P.-L. Taberna, P. Simon, M.R. Palacín, On the origin of the extra capacity at low potential in materials for Li batteries reacting through conversion reaction, Electrochim. Acta 61 (2012) 13–18.
[52] Y. Wang, J. Wu, Y. Tang, X. Lu, C. Yang, M. Qin, F. Huang, X. Li, X. Zhang, Phase-controlled synthesis of cobalt sulfides for lithium ion batteries, ACS Appl. Mater. Interfaces 4 (8) (2012) 4246–4250.
[53] D. Cui, Z. Zheng, X. Peng, T. Li, T. Sun, L. Yuan, Fluorine-doped SnO 2 nanoparticles anchored on reduced graphene oxide as a high-performance lithium ion battery anode, J. Power Sources 362 (2017) 20–26.
[54] M. Li, X. Yang, C. Wang, N. Chen, F. Hu, X. Bie, Y. Wei, F. Du, G. Chen, Electrochemical properties and lithium-ion storage mechanism of LiCuVO4 as an intercalation anode material for lithium-ion batteries, J. Mater. Chem. 3 (2) (2015) 586–592.
[55] G. Yoon, D.-H. Kim, I. Park, D. Chang, B. Kim, B. Lee, K. Oh, K. Kang, Using first-principles calculations for the advancement of materials for rechargeable batteries, Adv. Funct. Mater. 27 (40) (2017) 1702887.
[56] Y.-R. Luo, Comprehensive Handbook of Chemical Bond Energies 1st Edition, CRC Press, 2007.
[57] Y. Zhang, H. Wang, B. Wang, H. Xu, H. Yan, M. Yoshimura, Hydrothermal synthesis of metastable γ-manganese sulfide crystallites, Opt. Mater. 23 (1–2) (2003) 433–437.
[58] C.F. Liu, C.K. Zhang, H.Q. Song, C.P. Zhang, Y.G. Liu, X.H. Nan, G.Z. Cao, Mesocrystal MnO cubes as anode for Li-ion capacitors, Nanomater. Energy 22 (2016) 290–300.
[59] Y. Tang, S. Chen, S. Mu, T. Chen, Y. Qiao, S. Yu, F. Gao, Synthesis of capsule-like porous hollow nanonickel cobalt sulfides via cation exchange based on the Kirkendall effect for high-performance supercapacitors, ACS Appl. Mater. Interfaces 8 (15) (2016) 9721–9732.
[60] C.F. Liu, C.K. Zhang, H.Q. Song, X.H. Nan, H.Y. Fu, G.Z. Cao, MnO nanoparticles with cationic vacancies and discrepant crystallinity dispersed into porous carbon for Li-ion capacitors, J. Mater. Chem. 4 (9) (2016) 3362–3370.
[61] M.S. Javed, J. Chen, L. Chen, Y. Xi, C. Zhang, B. Wan, C. Hu, Flexible full-solid state supercapacitors based on zinc sulfide spheres growing on carbon textile with superior charge storage, J. Mater. Chem. 4 (2) (2016) 667–674.
[62] M.S. Javed, S. Dai, M. Wang, Y. Xi, Q. Lang, D. Guo, C. Hu, Faradic redox active material of Cu7S4 nanowires with a high conductance for flexible solid state supercapacitors, Nanoscale 7 (32) (2015) 13610–13618.
[63] M.S. Javed, S. Dai, M. Wang, D. Guo, L. Chen, X. Wang, C. Hu, Y. Xi, High performance solid state flexible supercapacitor based on molybdenum sulfide hierarchical nanospheres, J. Power Sources 285 (2015) 63–69.
[64] C.X. Guo, C.M. Li, A self-assembled hierarchical nanostructure comprising carbon spheres and graphene nanosheets for enhanced supercapacitor performance, Energy Environ. Sci. 4 (11) (2011) 4504.

[65] Y. Wang, Z. Shi, Y. Huang, Y. Ma, C. Wang, M. Chen, Y. Chen, Supercapacitor devices based on graphene materials, J. Phys. Chem. C 113 (30) (2009) 13103–13107.
[66] H. Kim, M.-Y. Cho, M.-H. Kim, K.-Y. Park, H. Gwon, Y. Lee, K.C. Roh, K. Kang, A novel high-energy hybrid supercapacitor with an anatase TiO2-reduced graphene oxide anode and an activated carbon cathode, Advanced Energy Materials 3 (11) (2013) 1500–1506.
[67] E. Lim, H. Kim, C. Jo, J. Chun, K. Ku, S. Kim, H.I. Lee, I.-S. Nam, S. Yoon, K. Kang, J. Lee, Advanced hybrid supercapacitor based on a mesoporous niobium pentoxide/carbon as high-performance anode, ACS Nano 8 (9) (2014) 8968–8978.